ESA Contract Report

ESA contract 4000130590/20/NL/IA

Contract Report to the European Space Agency

WP-2000 Calibration of EDA spread and adaptation of the observation error model

Technical Note 2 (final version) for ESA contract no. 4000130590/20/NL/IA

Authors: Katie Lean, Niels Bormann and Sean Healy

April 2021

Series: ECMWF ESA Contract Report Series

A full list of ECMWF Publications can be found on our web site under:
http://www.ecmwf.int/en/publications/

Contact: library@ecmwf.int

European Centre for Medium Range Weather Forecasts, Shinfield Park, Reading, RG2 9AX, UK

Contents

Abstract

In this second phase of this project to investigate potential future constellations of small satellites carrying microwave (MW) sounding instruments, there are two subjects that have been explored. In the first part of this report, real MW data have been used to establish links between the observation impact using the Ensemble of Data Assimilations (EDA) method, described in the initial consolidation phase, and in Observing System Experiments (OSEs). Reductions in the EDA spread, which indicate a positive impact from the MW data, were compared with reductions in the standard deviation of forecast error. The forecast error has been evaluated by comparing the short-range forecast to a reference firstly provided by analyses from the operational system and secondly by radiosonde observations, taking into account the observation error. There is overall good qualitative similarity between EDA spread and both measures of the forecast error. Better agreement of the observation impact is found in the lower/mid-troposphere with possible under-estimation of the impact using the EDA spread in the stratosphere. While it is not useful to derive a quantitative relationship here, the results show that the EDA method provides a basis to investigate the relative impacts from the future simulated small satellite data and with the addition of reference points from the use of existing MW data.

The second part of the report presents the adaptation of the observation error model for the MW temperature sounding channels needed due to the unavailability of key low frequency channels on the small satellites. For channels with cloud sensitivity, the observation error model for the all-sky assimilation inflates the observation error in cloudy regions by using an indicator of the presence of cloud in the observations or model. The use of the 52.8GHz (channel 4 on AMSU-A) has been proposed as the basis to construct an alternative cloud indicator for MW temperature sounding channels. Evaluation using AMSU-A observations showed that a similar structure to the current observation error model can be achieved with the new indicator. Assimilation experiments showed some small but significant negative impacts in short-range forecasts as measured by low peaking temperature sounding channels of ATMS. There is also a small but not significant signal in some humidity sensitive observations, however, impacts were generally neutral. Neutral impacts at longer forecast lead times measured by verification against analyses showed that these short-range changes did not affect the medium-range forecasts. The results confirm that 52.8GHz provides a viable alternative to use for the small satellite temperature sounding observation error model. However, it is noted that the potential impact from the loss of the lower frequencies is not fully captured as the channels are not currently used in the operational assimilation of AMSU-A.

1 Introduction

Recent advances in technology have allowed the possibility of launching microwave (MW) sounding instruments on small satellites with a performance that is expected to be satisfactory for the requirements of Numerical Weather Prediction (NWP). These small satellites are expected to become an important component of the future observing system and complement the continued use of instruments on a core constellation of larger platforms. This project aims to investigate different potential future constellations of small satellites carrying MW sounding instruments. How much further benefit could be achieved with even better temporal sampling from additional instruments will be established while considering practicalities such as instrument limitations and cost in order to determine an optimal design for global Numerical Weather Prediction (NWP).

The impact of these possible constellations will be evaluated by the Ensemble of Data Assimilations (EDA) method. The EDA consists of running a finite number of independent cycling assimilation systems, in which observations and the forecast model are perturbed to generate different inputs for each member. The small satellite data will be simulated using ECMWF operational analyses with the orbital parameters required for different constellation scenarios being provided by ESA. Accompanying obser-

vation errors will also be simulated for the small satellite data. In the EDA experiments, the simulated data are used in addition to the full observing system but with a slightly reduced number of existing MW sounders, representing a realistic future baseline. The benefit from adding the new data is measured by reducing the spread of the ensemble members which reflects improvement to the uncertainties in analyses and forecasts. Further details of the EDA methodology and outline of the data simulation framework, including a list of orbital parameters required as input, can be found in Lean et al. (2021).

Lean et al. (2021) also concluded that for robust statistics, EDA experiments would be run for a period of four weeks. Without the requirement to run for longer, more computationally expensive periods, this allowed the proposal of ten different constellation scenarios for testing. The choice of scenarios is expected to evolve through discussions between ECMWF and ESA with the aim of reaching a final list by the end of October 2021. The following key themes form the motivation for the scenarios chosen:

- What is the optimal number of satellites and their orbit type (e.g. polar or low inclination orbits)?
- What sets of channels (humidity and/or temperature sounding) provide the most benefit?
- What are the effects from other limitations in instrument performance, such as poorer instrument noise?

Building on the earlier consolidation work, in this second phase of the project we continue preparatory work to relate the changes in spread in the EDA experiments to impacts measured by Observing System Experiments (OSEs), using existing observations in both cases. In OSEs, the impact of an observing system is measured by how it reduces the forecast error, i.e. the difference between forecasts and a reference. The reference is typically an analysis produced by an NWP system, or a set of observations, such as radiosondes. A reduction in the standard deviation of the differences between forecasts and the reference between experiment and control indicates an improvement. Results from both options, using analysis and observation-based references, are presented in this report.

This comparison between EDA and OSE impacts for existing observations is sometimes referred to as a calibration step, but the aim here is not to infer an exact, quantitative relationship. Rather, this step provides evidence of the strong links between a reduction in the EDA spread and a reduction in the standard deviation of forecast error seen in OSEs. It confirms the change in EDA spread as an appropriate means to measure observation impact and gives confidence in the reference points using real data against which the addition of the small satellite data can be compared. It can be useful in particular to assess systematic effects on the EDA spread, for example, resulting from an under-dispersive ensemble. In this case, the ensemble spread is smaller than the corresponding forecast error which is a known characteristic (Bonavita et al., 2012) for example, relating to imperfect generation of the perturbations for each ensemble member. Results from Harnisch et al. (2013) supported the under-dispersive nature of the EDA although the forecast error reductions from the OSEs were found to be in good agreement with the reductions in the EDA spread.

In this report we will also consider adaptation of the observation error model that will be used for the small satellite data. The simulated MW data will be used in an all-sky framework where the observation error is linked to an estimate of the amount of cloud affecting the observation (Geer et al., 2014; Weston et al., 2019). Currently, the error model for temperature sounding channels around 54-57GHz includes use of lower frequency channels at 23.8GHz and 31.4GHz to identify the cloud amount. However, due to the compact technology on the small satellite, these lower frequencies will not be available. Using AMSU-A observations, we develop and test an alternative observation error model for the temperature-sounding channels, using only the channels expected to be available from a MW sounder on a small satellite.

Table 1: Details of satellites and their respective temperature and humidity sounding instruments included in the baseline EDA experiment to which different configurations of simulated small satellite observations will be added (ECT = approximate equator crossing time of descending node)

Satellite	Temperature sounding	Humidity sounding	ECT
Metop-A	AMSU-A	MHS	09:30
Metop-B	AMSU-A	MHS	09:30
NOAA-15	AMSU-A	-	06:30
DSMP F-19	-	SSMIS	06.30
NOAA-18	AMSU-A	MHS	08.00
NOAA-19	AMSU-A	MHS	04.00
NOAA-20	ATMS	ATMS	01:30
SNPP	ATMS	ATMS	01:30

This report will accordingly be split into two parts. In section 2 we present the comparison between the EDA and OSE impacts, starting with a brief review of the experiment configurations and data usage. This is followed by discussion of the links between EDA spread and standard deviation of forecast error and then the change in EDA spread compared to radiosonde fit. For the second topic, section 3 will consider the adaptation of the error model to replace use of lower frequency channels with a indicator of cloud based on the 52.8GHz channel. After an overview of the current error model, the proposed structure of the alternative model is presented. Results from assimilation experiments to test the performance of the new indicator are discussed. Section 4 summarises the conclusions of both parts and the implications for testing the simulated small satellite data.

2 Relationship between EDA and OSE impact

2.1 EDA and OSE configurations

In Lean et al. (2021) data were analysed from two EDA experiments which compared a control where no MW sounders were assimilated against a "7-sounders" experiment using a selection of operational MW sounding instruments that could represent a future baseline for the addition of the small satellites. The experimentation takes advantage of the presently available constellation of MW sounding instruments, which benefits from many old satellites still operating beyond their design life. In the 7-sounders experiment, 7 pairings of temperature and humidity sounding instruments across several satellite platforms were carefully chosen to distribute temperature and humidity sounding capabilities as evenly as possible in a variety of orbits, within the constraints of the current observing systems. Table 1 provides a reminder of the instruments used. The investigation showed that after a spin-up of about one week, the 7-sounders experiment showed a robust reduction in the EDA spread. In the following, we will assess how this reduction relates to measures of forecast error reduction seen in OSEs in which the same existing observations are added. The OSEs used are part of a wider study which systematically looked at the incremental introduction of 1, 3, 5, and 7 MW humidity and temperature sounders, highlighting the continued benefit obtained (Duncan and Bormann, 2020).

Both EDA and OSEs were run from 1st Jun - 15th Sept 2018. The EDA configuration employed a $T_{Co}399$ (25km) resolution grid with 137 vertical levels and three inner loops at a resolution of TL95/TL159/TL255.

The OSE accounts for the change in background error due to the changed observing system by making use of the background error estimates from the updated EDA. The OSE experiments were run at a higher resolution of $T_{Co}639$ ($\sim$18km) resolution grid with 137 vertical levels and three inner loops at resolution of TL255/TL319/TL399. The EDA comprises the control run and 10 perturbed ensemble members as described previously. Following Lean et al. (2021) the first week of the EDA experiments is discarded in our analysis due to the spin up time of the system. Note that for future EDA experiments to test the small satellite data, it was established previously that a total of four weeks would be enough to produce robust statistics. For OSEs, longer periods are required for analysis so statistics are calculated over the whole period for both although a shorter EDA time interval would give the same conclusions.

At very short forecast lead times (T+12, T+24), the evaluation of forecast errors with analyses can be problematic, as errors in the analyses and forecasts have comparable magnitudes, and errors in the analyses and forecasts can be highly correlated (Bormann et al., 2019). This was noted as a challenge by Harnisch et al. (2013) when using the EDA to evaluate the impact of additional Global Navigation Satellite System (GNSS) Radio Occultation (RO) observations. For the evaluation of short-range forecasts, observations are hence often used as a reference instead. In the following, we will first compare EDA spread reductions with forecast error reductions as determined through verification with analyses from the operational system, followed by a similar investigation, but using sonde observations as verification reference for the OSEs.

2.2 Analysis-based verification

To best capture the signal of the observation impact, very short lead times are recommended for calculation of the EDA spread to avoid the growing model uncertainties that reduce the clarity of signals at longer forecast ranges (Harnisch et al., 2013). Therefore the 12-hour forecast range is used to compare the reductions in EDA spread and forecast error in this study. In the calculation of the corresponding standard deviation of forecast error from the OSEs, the operational system is chosen to supply the verifying analyses. Figure 1 compares the mean change in EDA spread for temperature with the corresponding standard deviation of the forecast error for the control and 7-sounder experiments. There is good agreement throughout the vertical profiles with the EDA values closely following the pattern of the OSE values where the background errors are smaller in the mid-/upper-troposphere before increasing in the stratosphere. The values for the controls are also clearly larger than the respective experiments indicating the benefit of the MW data in both systems.

Other key variables considered for the impact of the MW data are the wind (originating from the tracing effect of the humidity radiances and other balance relationships) and the geopotential height at 500hPa which is used as an important parameter in measuring NWP performance. Figure 2 gives representative examples for the vertical profile of geopotential height and u component of wind. For geopotential height the values of EDA spread are noticeably smaller than the standard deviation of forecast error. This could be a reflection of the EDA being under-spread (Bonavita et al., 2012), due to, for example, imperfections in the perturbation generation or the finite ensemble size, but it could also be due to limitations in the estimation of the forecast errors in the OSEs, as further discussed below. Conversely, in the lower troposphere for the northern hemisphere u component, the EDA shows a more over-dispersive characteristic. However, in general, the pattern in the standard deviation of forecast error as measured by verification against the operational analysis is well replicated by the EDA spread.

As mentioned earlier, the estimation of short-range forecast errors using analyses can be problematic, as the size of the errors in the analyses and forecasts is comparable and taking full account of the errors in the analysis is largely impossible. This aspect is likely to affect the results presented in this section. When a

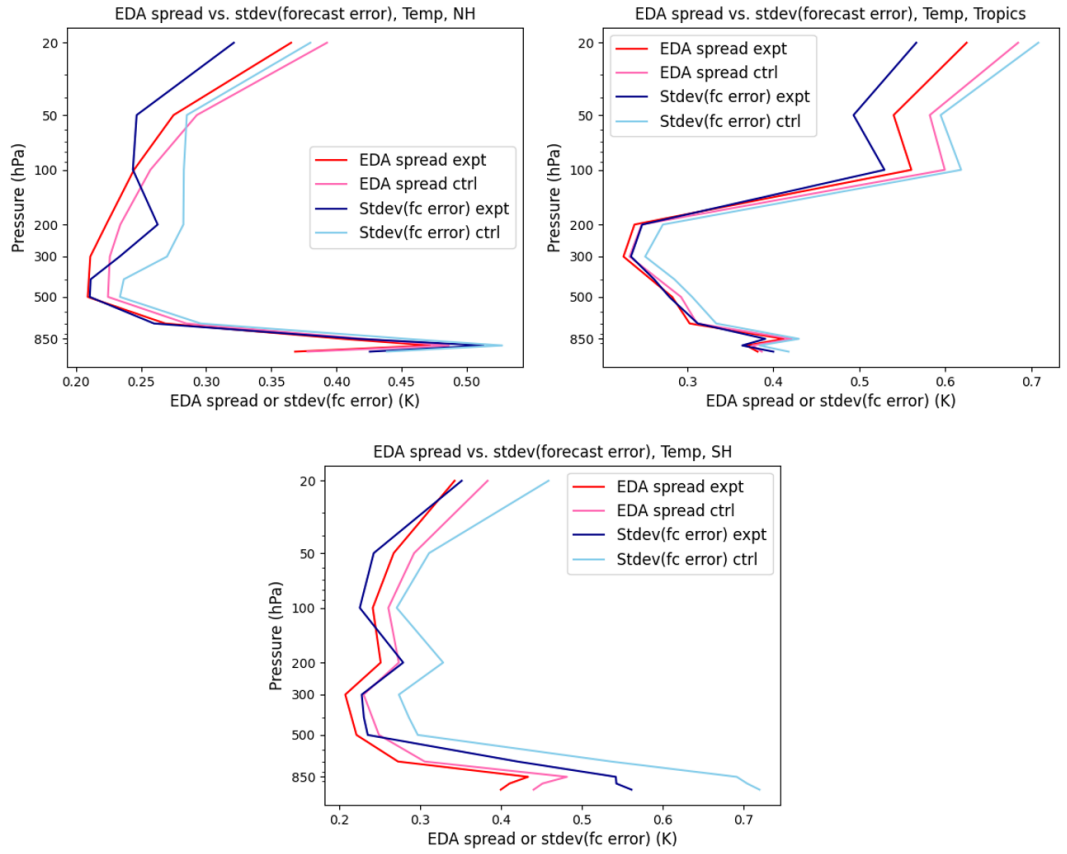

Figure 1: Vertical profiles of EDA spread and standard deviation of the forecast error of temperature for the control and 7-sounder experiments. Operational analyses are used as a reference for calculation of the forecast error. Data are averaged over the northern hemisphere (top left), tropics (top right) and southern hemisphere (bottom) and for the period 8th June - 15th Sept 2018.

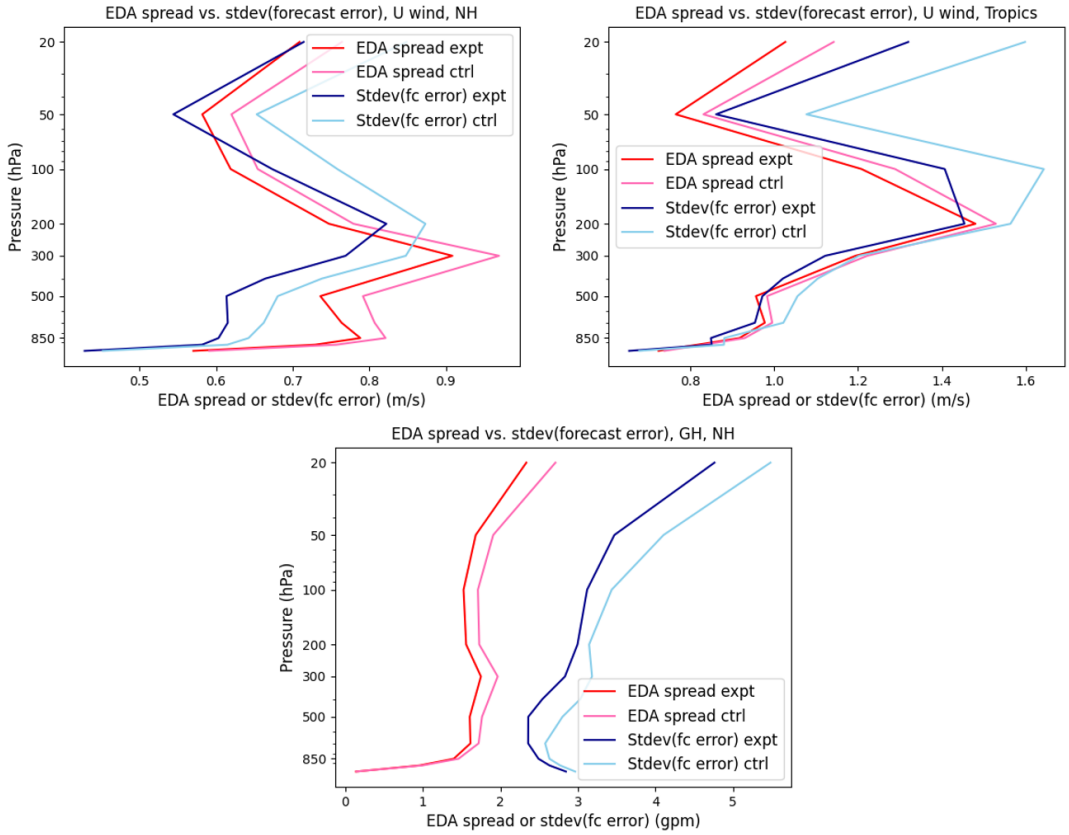

Figure 2: Vertical profiles of EDA spread and standard deviation of the forecast error of northern hemisphere (top left) and tropical (top right) u component wind and northern hemisphere geopotential height (bottom) of for the control and 7-sounder experiments. Operational analyses are used as a reference for calculation of the forecast error. Data are for the period 8th June - 15th Sept 2018.

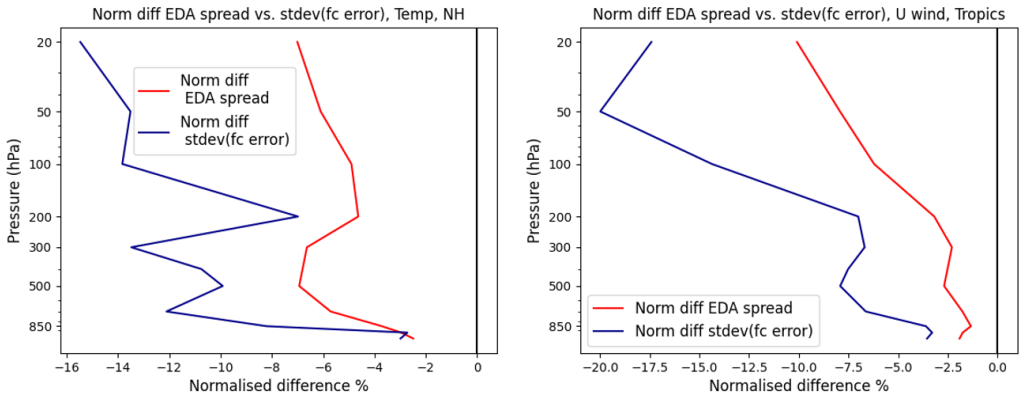

Figure 3: Vertical profiles of percentage normalised difference of EDA spread and standard deviation of the forecast error of northern hemisphere temperature (left) and tropical U wind (right) for the control and 7-sounder experiments. Operational analyses are used as a reference for calculation of the forecast error. Data are averaged over the period 8th June - 15th Sept 2018.

large component of the observing system is removed, the operational system provides the best reference analysis for comparison, but it likely overestimates the impact due to more similarity in errors between the operational analysis and 7-sounder experiment where the observing systems are closer. Conversely, if each experiment is verified against its own analysis, there can be correlated errors between the analysis and short-range forecasts that may lead to underestimation of the impact. Indeed when the normalised differences were calculated here, the OSE impact was consistently larger (often by a factor of 1.5-2 times) than the EDA spread change when using the operational analyses as reference as illustrated in the representative plots in figure 3. Despite the magnitude difference, the overall vertical profile generally shows similarity such as more reduction in the stratosphere. The opposite effect, with the EDA spread change being of larger magnitude, is found using own-analysis verification (not shown). Harnisch et al. (2013) noted a similar limitation when comparing their EDA experiments and OSEs. To address this, in the next section we instead consider the links between the EDA spread changes and forecast error reduction as estimated through comparisons to observations.

2.3 Observation-based verification

To avoid the difficulties in interpreting the observation impact due to the verifying analysis, the EDA spread change has also been compared to the reduction in the standard deviation of differences between radiosondes and short-range forecasts. These differences are often referred to as O-B where B, the model background, is the 12-hour forecast from the previous model cycle. Such comparisons are also not free from difficulties. Firstly, radiosondes do not sample the globe homogeneously, and in particular do not capture well forecast quality over oceans or other remote areas. Secondly, the effect of observation errors has to be taken into account when comparing observation-based forecast error estimates, as it is a sizeable component of the differences between forecasts and observations. Nevertheless, radiosonde verification provides an alternative way to estimate errors in short-range forecasts.

Due to the influence of the observation error, as will be shown later (figure 5), the magnitude of the change in radiosonde fit is much smaller than the EDA spread change. To address this, we use the change

in EDA spread and appropriate observation errors to estimate the expected impact on the radiosonde fit if the EDA and the observation error estimates correctly represent background and observation errors, respectively. This will then be compared to the values computed in the OSE verification against actual radiosondes. The standard deviation of radiosonde O-B can be calculated using the following equation with the assumption that observation error and background errors are uncorrelated:

$$Standard\,deviation(O-B) = \sqrt{\sigma_B^2 + \sigma_O^2} \tag{1}$$

Where, for this investigation, the background errors, σ_B are given by the EDA spread values and σ_O are the estimated radiosonde observation errors. By repeating this calculation for the control and experiment, the expected normalised difference for the radiosonde fit can be estimated and compared to the OSE values. The observation errors for the radiosondes have been provided by B. Ingleby (pers. comm., 2021). They have been generated over the period Nov 2016 - Feb 2017 using the Desroziers diagnostic technique (Desroziers et al., 2005) based on the Vaisala RS92 and RS41 radiosondes which are known to be a good quality instrument type (Dirksen et al., 2014; Ingleby, 2017).

Figure 4 shows the standard deviation of the temperature and u-wind radiosonde O-B statistics alongside the expected values that have been estimated from combining the EDA spread and Desroziers observation errors (equation 1). The vertical pattern in the EDA-based values is similar to the ones from the OSEs, consistent with the results from the analysis-based evaluation in the previous section. However, the EDA-based values are generally smaller. On the one hand, this could be an indication that the EDA is under-spread. On the other hand, it could also be due to an under-estimate of the observation error in the radiosondes, which is based on an estimate for a good quality radiosonde type whereas the average over all the radiosondes (as used in the OSE) may have larger errors. A further effect is that the EDA spread is an average over land and sea which may be lower compared to the radiosonde background values being used which primarily sample land areas. Nevertheless, the overall results confirm the impression that at least qualitatively the EDA represents well the errors in short-range forecasts.

Assessment of the corresponding normalised differences (figure 5) reveals that the values estimated by equation 1 provide a good approximation of the OSE impact. The EDA change in spread has also been plotted for reference but is clearly a different magnitude to the radiosonde impact if the observation error contribution is not accounted for. Not all of the vertical structure is captured by the estimated values and there are some small differences in the magnitude. The agreement tends to be better in the lower to mid-troposphere, whereas an under-estimation of the impact is apparent for the upper troposphere and stratosphere. However, considering the approximations discussed e.g. the underestimation of the observation error or coverage differences, there is overall very encouraging correspondence between the OSE impact and those generated using the EDA spread change.

In summary, within the uncertainties of forecast-error estimation, the reductions in the EDA spread resulting from adding existing observations compare favourably with reductions in forecast errors seen in OSEs. This is true for both analysis-based as well as observation-based estimates of the forecast error reduction in OSEs. At the same time, it is also clear that there is not a one-to-one correspondence, and at times the EDA spread reductions can be prone to under-estimating the impact seen.

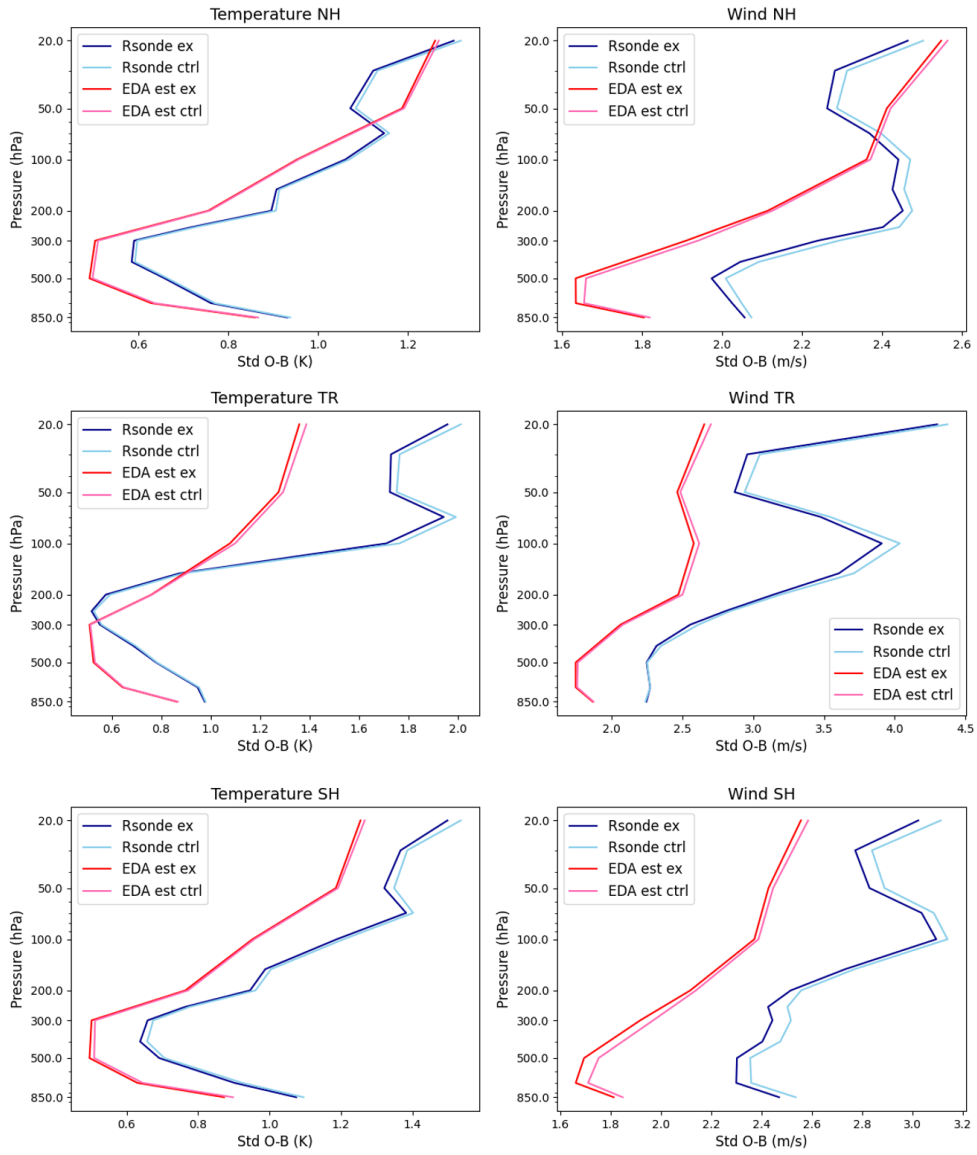

Figure 4: Standard deviation of observation - background departures for temperature (right column) and u wind component (left column) using values directly taken from the OSE verification and the estimates of the same statistics generated with equation 1 (using the EDA spread and Desroziers observation errors). Data are shown averaged over the northern hemisphere (top row), tropics (middle row) and southern hemisphere (bottom row) and from 8th Jun - 15th Sept 2018.

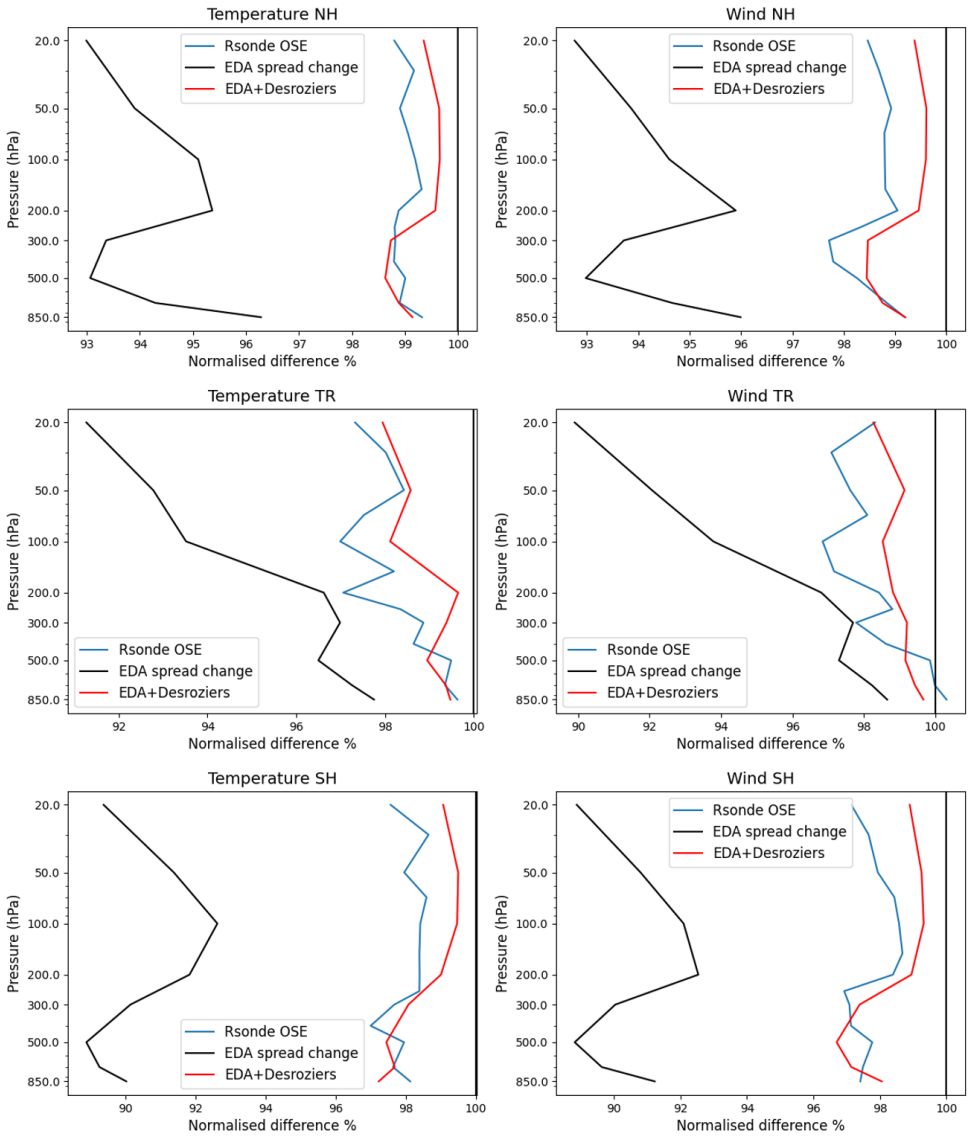

Figure 5: Normalised difference in the EDA spread and standard deviation of observation - background departures for temperature (right column) and u wind component (left column) using values directly taken from the OSE verification and the estimates generated with equation 1 using the EDA spread and Desroziers observation errors. Data are shown averaged over the northern hemisphere (top row), tropics (middle row) and southern hemisphere (bottom row) and from 8th Jun - 15th Sept 2018.

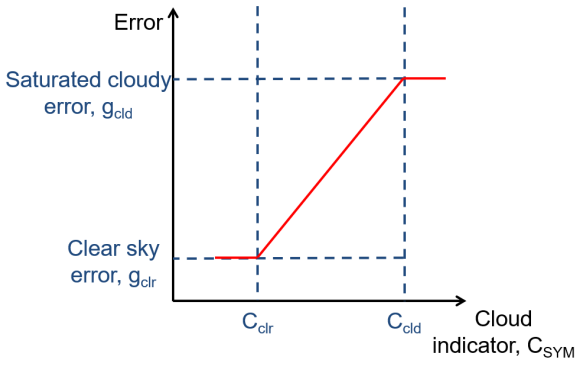

Figure 6: Simple schematic showing how the coefficients in equations 3 - 5 define the form of the error model.

3 Adapting the observation error model for the 50 GHz temperature-sounding channels

Simulated data from both humidity and temperature sounding channels on the small satellites will be used in the all-sky framework at ECMWF (Geer et al., 2010, 2017). At present, MW temperature sounding channels are not used in the all-sky mode operationally at ECMWF but implementation for AMSU-A is submitted for inclusion in the next operational upgrade. A key aspect of the all-sky assimilation of MW data is the modelling of observation errors. The observation error typically comprises of measurement error, such as originating from instrument noise, the forward model error, e.g. from the radiative transfer calculations, and representation error, arising from different scales and processes being represented in the observations and the model fields. In the case of all-sky use, the representation error dominates the observation error in cloudy conditions, arising from different representativeness of clouds in the observations and the model fields. This is accounted for by an observation error model that assigns larger observation errors in cloudy regions, based on a suitable indicator of the presence of clouds in the observations or the model fields (Geer and Bauer, 2011).

Key low frequency channels used in the error model developed for all-sky use of the AMSU-A temperature-sounding channels in the 50GHz-band will be unavailable on the small satellites. In the following, we hence develop an alternative error model, using the available 52.8GHz (channel 4 on AMSU-A) to design a cloud indicator. The observation error model is tested in assimilation trials to establish the performance compared to the previously developed model.

3.1 Current observation error model for temperature sounding observations in the 50 GHz band

The all-sky observation error used at ECMWF is formulated in terms of a cloud indicator, as indicated schematically in figure 6. For AMSU-A, there are two different cloud indicators used in the error model corresponding to land or ocean surfaces. Over land, the difference 23.8-89GHz provides a scattering index which exploits the increased scattering from frozen hydrometeors at 89GHz compared to 23.8GHz (Bennartz et al., 2002). Over ocean, the indicator is the retrieved liquid water path (Grody et al., 2001) which is derived from 23.8GHz and 31.4GHz channels.

The cloud indicator used in the error model is formulated by taking the average of the cloud indicator values for the observations and the model background:

$$C_{SYM} = (P_{obs} + P_{bkrd})/2 \tag{2}$$

Where P_{obs} is the indicator calculated using observed values e.g. the difference in observed brightness temperatures at 23.8 and 89 GHz for the scattering index and P_{bkrd} is calculated using the model background equivalent brightness temperatures. The final observation error is then constructed with either a linear or quadratic dependence on the cloud indicator as the following (reproduced in the linear form using the same notation from Geer et al. (2014)):

$$g_{clr} \in C_{SYM} <= C_{clr} \tag{3}$$

$$g(C_{SYM}) = g_{clr} + (g_{cld} - g_{clr}) \left(\frac{C_{SYM} - C_{clr}}{C_{cld} - C_{clr}} \right) \in C_{clr} < C_{SYM} < C_{cld} \tag{4}$$

$$g_{cld} \in C_{SYM} >= C_{cld} \tag{5}$$

Where g_{clr} and g_{cld} are the clear sky and saturated cloudy error values respectively while C_{clr} and C_{cld} are threshold values of the symmetric cloud indicator to separate clear and saturated cloudy situations, respectively. The clear sky values reflect the individual channel noise estimates of the instrument, inflated in recognition of other error sources in this situation e.g. from forward modelling error. The cloudy saturation value and the choice of a linear or quadratic nature of the model are determined by analysing the standard deviation of background departures binned as a function of the symmetric cloud indicator (e.g. fig 7). These values are determined separately for each satellite and individual instrument channels. Figure 6 illustrates how the coefficients define the construction of the error model.

Currently AMSU-A channels 5 - 9 all use this error model to increase errors in cloudy situations. As the channel number increases, the height of the peak sensitivity also increases (with the channel 9 peak of the weighting function around 80-90hPa) and correspondingly the impact of cloud decreases. This means that the difference between the clear sky (g_{clr}) and saturated cloudy values (g_{cld}) gradually reduces with increasing channel number. For channel 10 and above, the impact of cloud is negligible so the error model becomes a constant value given by g_{clr}.

Figure 7 uses Metop-C as an illustrative example of the current error model (derived using data sampled from June - Sept 2019 and Dec 2019 - Mar 2020, D. Duncan, pers. comm., 2020) and the variability of background departures over land and ocean surfaces where data are from 1st - 10th Dec 2020. The vast majority of the data are located close to or at the clear sky situation and the number of observations falls rapidly as the predicted cloud amount increases. In this example, both land and sea cases show the standard deviation of O-B following a quadratic dependence on C_{SYM} which is reflected in the error model. However, there is a mixture of quadratic and linear relationships diagnosed across the channels (not shown). The standard deviation also appears to plateau for the LWP indicator leading to the choices of C_{cld} and g_{cld}. For the land-based observations, the error model slightly underestimates the O-B standard deviation which may be linked to the different period of analysis and could be highlighting the weakness with detecting liquid water cloud/precipitation.

3.2 Use of 52.8GHz as a cloud indicator

One of the limitations of the compact instrument design on the small satellite will be the unavailability of channels with frequencies less than 50GHz. This means the absence of channels contributing to both the

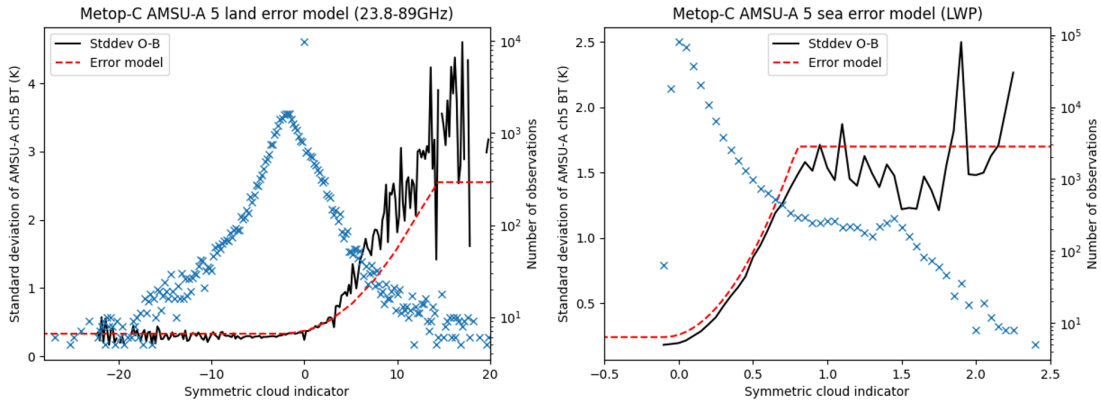

Figure 7: Standard deviation of observation - background departures for Metop-C AMSU-A ch5 binned as a function of the symmetric cloud indicator. Left panel shows land points where the 89-23GHz scatter index is used as the cloud indicator, right panel shows sea points where LWP is used. Crosses indicate the number of observations in each bin. Data are from 1st -10th Dec 2020, limited to $\pm 60^{\circ}$N to exclude sea ice contamination and are actively used observations taken from an experiment assimilating AMSU-A in an all-sky framework.

land and sea-based error models. In the following, we will use an alternative cloud indicator, following an approach that has been previously suggested by Okamoto et al. (2014) for all-sky assimilation of infrared radiances. The new cloud indicator measures the cloud effect in a window channel, and the available 52.8 GHz channel is used for this purpose (i.e. AMSU-A channel 4). The cloud effect in the model background can be expressed as the absolute difference between the equivalent brightness temperature from the model background using the cloudy radiative transfer model, BT_{ch4cld}, and the clear sky calculation for the same model background (BT_{bkclr}). The cloud effect in the observation is estimated similarly by taking the absolute difference between the actual observations, BT_{ch4obs}, and the simulated clear sky brightness temperature from the model background. The symmetric cloud indicator from equation 2 can now be written as:

$$C_{CH4SYM} = (\text{abs}(BT_{ch4obs} - BT_{bkclr}) + \text{abs}(BT_{bkcld} - BT_{bkclr}))/2 \tag{6}$$

The new cloud indicator can be applied over land as well as over sea. For observation error modelling over land, Weston et al. (2019) suggested such an indicator may actually be advantageous compared to the scatter index presently used. The current scattering index is mainly sensitive to frozen hydrometeors and less able to detect cloud liquid water and precipitation which is actually the dominant influence on AMSU-A channel 5 (53.596 $\pm$ 0.115GHz). A channel 4 departure-based check has been used in screening cloud in the clear-sky and, like channel 5, is also primarily sensitive to cloud liquid water and rain.

Using illustrative examples from AMSU-A on Metop-C, figure 8 shows the standard deviation of AMSU-A channel 5 binned as a function of C_{CH4SYM} over land and ocean surfaces. The error model has been fitted by eye, providing values for the coefficients for g_{cld}, C_{clr} and C_{cld} described in equations 3 - 5. The clear sky error value remains the same in both error models. There is a strong linear relationship between the standard deviation and C_{CH4SYM}, which is present for channels 6 - 9 as well (not shown), giving a good basis for the error model. The number of observations, similar to figure 7, is very large at low standard deviations/clear sky situations and falls rapidly.

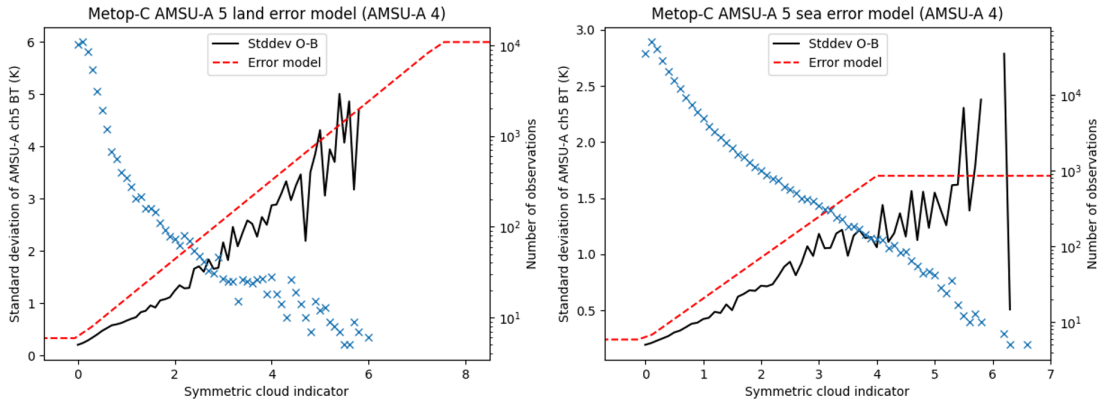

Figure 8: Standard deviation of observation - background departures for Metop-C AMSU-A ch5 binned as a function of the symmetric cloud indicator using AMSU-A channel 4. Left panel shows land points, right panel shows sea points and crosses indicate the number of observations in each bin. Data are from 1st -10th Dec 2020, limited to $\pm 60^{\circ}$N to exclude sea ice contamination and are actively used observations taken from an experiment assimilating AMSU-A in an all-sky framework.

Table 2: Values for Metop-C coefficients used in the observation error model over land

AMSU-A channel	g_{clr}	g_{cld}	C_{clr}	C_{cld}
5	0.33	6.0	0	7.5
6	0.18	2.0	0	9.0
7	0.19	0.6	0	9.0
8	0.20	0.35	0	10.0
9	0.20	0.27	0	8.0

For ocean surfaces, the values for the saturated cloudy error situations (g_{cld}) derived using the LWP indicator are also appropriate here with the standard deviation values similarly showing indications of plateauing. For land surfaces, the decision was taken to raise the value of g_{cld} to account for the continued linear increase in standard deviation at high values of C_{CH4SYM}. In practice though, very few observations will be assigned these values. In all the channels, by design, the error model is slightly over-estimating the O-B standard deviation values. In data assimilation it is safer to over- rather than under-estimate the observation errors - with errors that are too small it is possible to produce an analysis solution which is degraded from the initial background input.

Table 2 and 3 give the values for the coefficients for Metop-C AMSU-A. The clear-sky values for other satellites show some variations, reflecting different noise performances for different instruments, whereas the saturation values for the cloudy part are relatively similar across the different satellites. For application to the small satellites, it is expected that instrument noise performance is similar to the current AMSU-A instruments. Therefore, for the clear sky coefficients in the error model, the noise equivalent delta temperature (NEDT) will be compared to the AMSU-A noise levels and the same scaling applied to reach g_{clr} values. The resulting error model will then be based on e.g. Metop-C (as a newer satellite where all the AMSU-A channels are working well) and g_{cld} shifted according to the clear sky start point.

Table 3: Values for Metop-C AMSU-A coefficients used in the observation error model over sea

AMSU-A channel	g_{clr}	g_{cld}	C_{clr}	C_{cld}
5	0.24	1.7	0	4.0
6	0.17	0.54	0	4.0
7	0.18	0.25	0	4.0
8	0.19	0.21	0	3.0
9	0.19	0.22	0	4.0

Note that an alternative cloud indicator is only being explored for the temperature sounding channels. For humidity sounding channels, the corresponding error model utilises channels at 89GHz and 150GHz (Geer et al., 2014) which both remain available in the small satellite configuration. Differences in scattering from precipitation-sized ice particles are exploited, similar to the current land scattering index model for temperature sounding channels. This makes it very suited to the 183GHz channels where frozen particles dominate the scattering (Lui, 2008; Geer and Baordo, 2014). As outlined above, AMSU-A channel 5 is affected more by cloud/precipitation in the liquid phase so use of the error model for humidity channels would not have been appropriate.

3.3 Assimilation experiments

The previous section has shown that the use of AMSU-A channel 4 as a cloud indicator allows us to derive an error model which can be closely linked to the variability in the standard deviation of the O-B statistics. To best assess the feasibility of the new cloud indicator, the next step is to test these coefficients in an assimilation experiment to ensure that we do not significantly degrade the impact of the AMSU-A temperature-sounding observations in the 50GHz band. For example, one of the drawbacks of the channel 4 departure-based cloud indicator is the potential correlations with the other low peaking channels that arise from similar radiative transfer errors affecting multiple channels. The aim is to be able to retain a significant proportion of the impact of the all-sky use of temperature sounding channels and accept that we will not be able to perfectly replicate the performance of the current model.

3.3.1 Experimental set up

Three assimilation experiments have been run which consist of:

- Control: uses the full observing system but does not assimilate any AMSU-A observations
- Experiment 1: the same configuration as the control but introduce AMSU-A all-sky observations using the current error model
- Experiment 2: the same configuration as the control but introduce AMSU-A all-sky observations using the new channel 4 based error model

In experiment 1 the original indicators are exclusively used and similarly for experiment 2 there is no mix of indicators being used in the error models. To achieve this, only satellite platforms were included where the channels needed for the original and channel 4 indicators are available and retain good performance.

As a consequence, the presence of broken channels that are key to one or both of the indicator schemes meant that the AQUA satellite was entirely removed and Metop-B restricted to use only over the sea in both experiments. Note that the 23.8 and 31.4 GHz channels from AMSU-A are not actively assimilated in any of the experiments above, so we only investigate their impact through the use in the observation error model. Similar channels are assimilated through an all-sky approach from conical scanners such as SSMI/S or AMSR2, but their assimilation for cross-track sounders such as AMSU-A and ATMS has not yet been developed in the ECMWF system. The experimentation presented here hence does not evaluate the full impact from the lack of the low-frequency channels on a future small satellite.

The experiments are all based on cycle 47R1 of the Integrated Forecast System (IFS) with the code modified to run AMSU-A in the all-sky framework with either the current or alternative channel 4 indicators used in the error model. The model resolution is $T_{Co}399$ ($\sim$25km) resolution grid with 137 vertical levels and 12-hour assimilation cycles. The experiments are run for two seasons covering 20th June - 12th Aug 2019 and 1st Dec 2019 - 21st Jan 2020 making a total of around 3.5 months.

3.3.2 Results

Globally, the number of AMSU-A observations used changes very little between the choice of cloud indicators. Different usage of the observations can arise as the assigned observation error plays a role in the quality control of the observations. More observations may be assimilated where the assigned observation errors are larger. There is an overall minor increase of the average assigned observation error, mostly around 10-30% over ocean and more variability over land with localised larger error changes (in excess of 60%) associated with areas experiencing small increases in observation number (not shown). A higher observation error may arise from a combination of a slightly more generous over inflation when determining the model slope, the increased cloudy saturation upper limit over land and using all linear rather than a mixture of quadratic and linear dependence on the indicator. Where the majority of data lie near the clear sky situation, small differences around this part of error model can affect a large number of observations.

When considering the change in the fit of independent observations to the model background, much of the impact is still retained with the new channel 4 indicator but there are small degradations also present. Figure 9 shows examples of the largest effects on Advanced Technology Microwave Sounder (ATMS) and the geostationary infrared radiances. ATMS is currently used in a clear sky only configuration but has a very similar temperature sounding channel set to AMSU-A and is therefore usually the most sensitive instrument to changes in AMSU-A use. ATMS channel 6, the equivalent to AMSU-A channel 5, shows a small but significant degradation when using the new indicator. The southern hemisphere, where microwave data tend to have greater impact in the absence of dense conventional data, shows the largest change of around 0.5%. The increase in the standard deviation of background departures suggests an increase in the short-range forecast error as seen by this channel. ATMS channels 7-9 and the humidity sounding channels 18-22 also indicate a signal of small negative impact. Changes in infrared radiances from geostationary imagers (figure 9) which are sensitive to water vapour features also show a tendency towards a less positive signal with the channel 4 cloud indicator.

Other observation groups such as the conventional data, show a very neutral response to the change. Figure 10 illustrates this point with the tropical U wind where the positive impacts in the upper troposphere are replicated when using the new indicator and there is no degradation introduced at higher pressures. Atmospheric Motion Vectors (AMVs) and the microwave imagers used in the all-sky framework all show a very neutral impact (not shown).

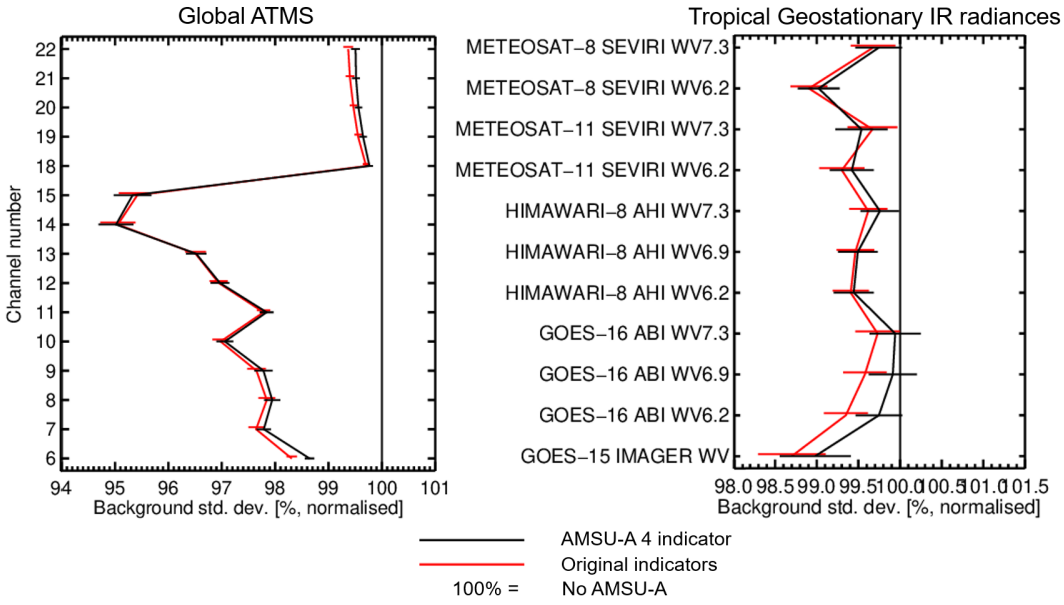

Figure 9: Change in the standard deviation of the observed - background brightness temperatures of ATMS over the global area (left) and geostationary imagers over the tropics (right) for the use of AMSU-A all-sky with the channel 4 cloud indicator (black) and original indicators (red) compared to the control with no AMSU-A. Data are from covering 20th June - 12th Aug 2019 and 1st Dec 2019 - 21st Jan 2020. Error bars indicate significance at the 95% level.

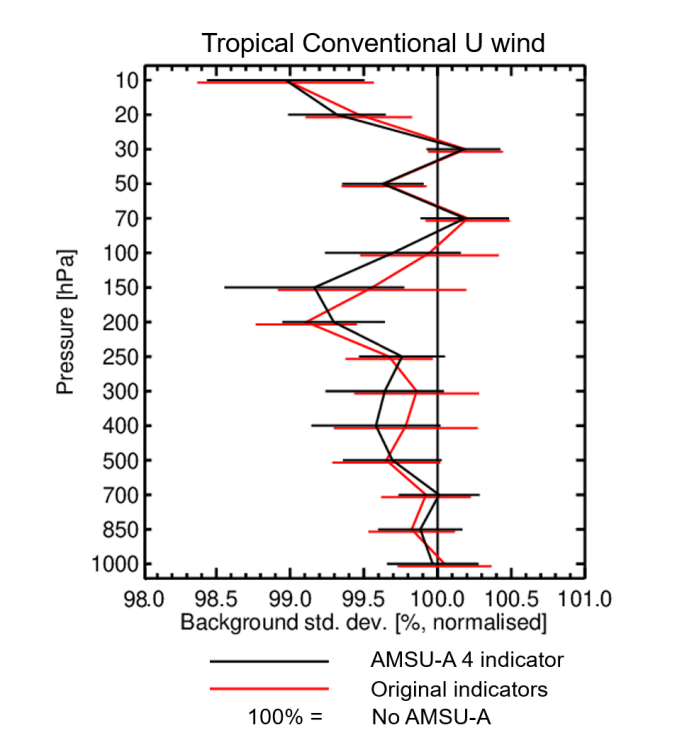

Figure 10: Change in the standard deviation of the observed - background U component of wind for conventional data in the tropics with the use of AMSU-A all-sky with the channel 4 cloud indicator (black) and original indicators (red) compared to the control with no AMSU-A. Data are from covering 20th June - 12th Aug 2019 and 1st Dec 2019 - 21st Jan 2020. Error bars indicate significance at the 95% level.

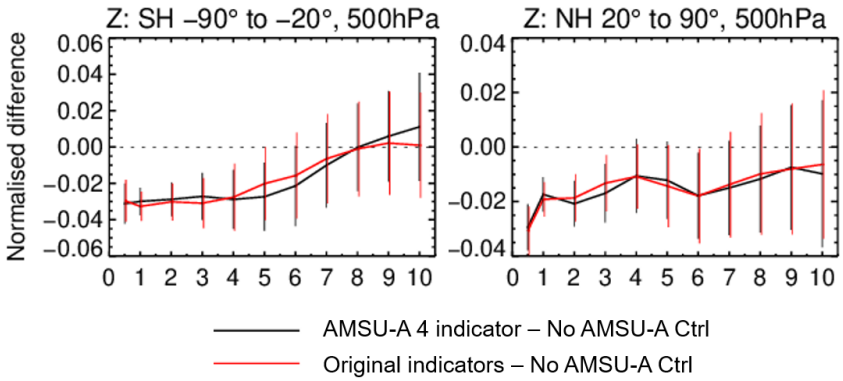

Figure 11: Normalised change in the geopotential height RMSE for different forecast ranges verified against own analysis for the northern hemisphere (right) and southern hemisphere (left). The experiments using the original cloud indicators (red line) and using the channel 4 indicator (black line) are verified against a control with no AMSU-A data. Data are from covering 20th June - 12th Aug 2019 and 1st Dec 2019 - 21st Jan 2020.

Although there are some small differences in the short-range forecast highlighted by the observation-based verification, they do not appear to translate into medium-range impacts. Figure 11 shows the normalised difference in geopotential height root mean square error (RMSE) for the experiments using the different indicators compared to the control baseline with no AMSU-A observations. There is very little to distinguish between the impacts from the two experiments. Similar plots of vector wind, temperature and humidity also reveal no significant impact from changing indicators (not shown). Maps and zonal plots of the differences that directly compare the two experiments together support the neutral signal. They also highlight that the performance is similar over land and sea (figure 12). A small but significant improvement in the temperature RMSE can be seen over equatorial Africa, possibly indicating even some local benefits from the new error model over land, as previously suggested by Weston et al. (2019).

In summary, the use of AMSU-A channel 4 as a cloud indicator in the error model is able to retain much of the positive impact seen in the current all-sky system making it a viable alternative that can be used for the small satellites. There are some small degradations suggesting that the performance of the original model is better however these are acceptably small.

4 Summary and discussion

In the second phase of the study for the optimal design of a prospective small satellite constellation with MW sounders, the focus has been on evaluating the relationship between the observation impact in the EDA experiments and the OSEs with existing observations, and secondly on the adaptation of the observation error model for the temperature sounding channels in the 50GHz band.

Comparison of the EDA spread values with standard deviations of estimates of forecast error revealed overall a good qualitative similarity in the vertical profiles for the main geophysical variables. This is true for evaluations of forecast error against operational analyses as well as against radiosonde observa-

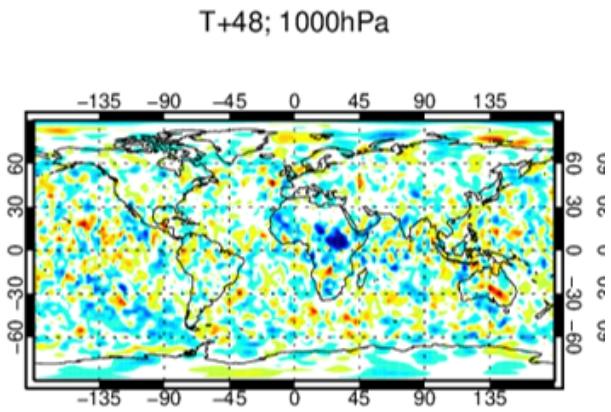

Figure 12: Map of the normalised change in the 1000hPa temperature RMSE verified against own analysis comparing the experiment using the channel 4 indicator directly against the experiment using the original indicators. Blue colours indicate improvements using the channel 4 indicator.

tions, and it is in line with the use of the EDA to estimate background errors for ECMWFs operational assimilation system (Bonavita et al., 2012).

The reductions in EDA spread resulting from adding observations are also found to be broadly consistent with forecast error reductions in corresponding OSEs when evaluated against radiosondes, provided radiosonde observation errors are taken into account. The agreement appears particularly good for the lower and mid troposphere, whereas the statistics suggest that the EDA may underestimate the impact in terms of temperature and wind in the stratosphere. Given uncertainties in the evaluation of short-range forecast errors, it is not considered useful to define a precise quantitative relationship here. However, overall, the results provide a good basis for interpreting EDA spread changes that will result from further addition of simulated future observations, ensuring that future EDA experiments to test the simulated small satellite data can be judged relative to the MW experiments already conducted with real data. Further research into calibrating the EDA spread against OSE impacts is currently also underway as part of a different ESA project looking into GNSS-RO data from the Spire satellites (Healy et al., 2020). Outcomes from this Spire study will be closely monitored and if necessary, the topic will be revisited here for the small satellites.

The second part of this report presented the adaptation and testing of the observation error model necessary for the MW temperature sounding channels in the 50GHz band due to the unavailability of low frequencies on the small satellites. AMSU-A data were used to successfully demonstrate that a cloud indicator based on AMSU-A channel 4 (52.8GHz) can be used to identify areas with larger differences between observations and background equivalents, reflecting larger representation errors in cloudy regions. The new cloud indicator allows the construction of an observation error model that closely follows the existing error model structure, and that can be adapted to reflect, for instance, different noise characteristics for future instruments. Assimilation experiments confirmed that while some degradations are noticeable in short-range forecasts, the impact of changing the observation error model is relatively small, and it is largely neutral in terms of medium-range forecast scores. This is an important result, as it ensures that we can expect good impact from the available channels from a small satellite, provided characteristics of the remaining channels are comparable to those of AMSU-A. Note, however, that our

experimentation does not measure the full impact of the lack of the low-frequency channels compared to heritage instruments, as our assimilation does not yet include the active assimilation of the 23.8 and 31.4 GHz channels of AMSU-A.

With the results presented in this report, we have concluded preparatory activities to establish important aspects of the use of the EDA, and to prepare for the treatment of errors in the future observations from small satellites. The next step of the study will be to develop the flexible simulation and assimilation of the new observations from a constellation of small satellites in ECMWFs Integrated Forecast System. This will follow closely the established use of all-sky assimilation for the relevant frequencies, with the adaptations in terms of the observation error modelling as outlined in the present report.

Acknowledgements

The authors would like to thank Bruce Ingleby for providing the observation error values for the radiosondes. The authors would also like to thank David Duncan for his assistance with technical details and discussion of the current all-sky error model and Elias Hòlm for discussion on aspects of the EDA.

References

Bennartz, R., Thoss, A., Dybbroe, A., Michelson, D., 2002. Precipitation analysis using the Advanced Microwave Sounding Unit in support of nowcasting applications. Met. Apps, 177–189.

Bonavita, M., Isaksen, L., Holm, E., 2012. On the use of EDA background error variances in the ECMWF 4D-Var. Quart. J. Roy. Meteorol. Soc 138 (667), 1540–1559.

Bormann, N., Lawrence, H., Farnan, J., 2019. Global observing system experiments in the ECMWF assimilation system. ECMWF Technical Memorandum No.839.

Desroziers, G., Berre, L., Chapnik, B., Poli, P., 2005. Diagnosis of observation, background, and analysis-error statistics in observation space. Q. J. R. Meteorol. Soc. 131, 3385–3396.

Dirksen, R. J., Sommer, M., Immler, F. J., Hurst, D. F., Kivi, K., V omel, H., 2014. Reference quality upper-air measurements: GRUAN data processing for the Vaisala RS92 radiosonde. Atmos. Meas. Tech. 7, 4463–4490.

Duncan, D. I., Bormann, N., 2020. On the Addition of Microwave Sounders and NWP Skill, Including Assessment of FY-3D Sounders. EUMETSAT/ECMWF Fellowship Programme Research Report No.55.

Geer, A., Baordo, F., Bormann, N., Chambon, P., English, S., Kazumori, M., Lawrence, H., Lean, P., Lonitz, K., Lupu, C., 2017. The growing impact of satellite observations sensitive to humidity, cloud and precipitation. Q.J.R. Meteorol. Soc. 143, 3189–3206.

Geer, A., Bauer, P., Lopez, P., 2010. Direct 4D-Var assimilation of all-sky radiances. Part II: Assessment. ECMWF Technical Memorandum No.619.

Geer, A. J., Baordo, F., 2014. Improved scattering radiative transfer for frozen hydrometeors at microwave frequencies. Atmos. Meas. Tech. 7, 1839–1860.

Geer, A. J., Baordo, F., Bormann, N., English, S., November 2014. All-sky assimilation of microwave humidity sounders. ECMWF Technical Memorandum No.741.

Geer, A. J., Bauer, P., 2011. Observation errors in all-sky data assimilation. Q. J. R. Meteorol. Soc. 137, 2024–2037.

Grody, N., Zhao, J., Ferraro, R., Weng, F., , Boers, R., 2001. Determination of precipitable water and cloud liquid water over oceans from the NOAA 15 advanced microwave sounding unit. J. Geophys. Res., 29432953.

Harnisch, F., Healy, S. B., Bauer, P., English, S. J., 2013. Scaling of GNSS Radio Occultation Impact with Observation Number Using an Ensemble of Data Assimilations. Mon. Wea. Rev. 141, 43954413.

Healy, S. B., Lonitz, K., Bowler, N., Marquardt, C., September 2020. Technical Note 1 for ESA Contract No. 4000131086/20/NL/FF/an: Impact Assessment of Commercial GNSS-RO data. ESA Contract 4000131086/20/NL/FF/an Technical Note 1 (unpublished), ECMWF, Reading, UK.

Ingleby, B., 2017. An assessment of different radiosonde types 2015/2016. ECMWF Technical Memorandum No.807.

Lean, K., Bormann, N., Healy, S., January 2021. Technical Note 1 for ESA Contract No. ESA RFP/3-16414/20/NL/IA: WP-1000 Review of EDA approach and recommendations for small satellite configurations. ESA Contract RFP/3-16414/20/NL/IA Technical Note 1 (unpublished), ECMWF, Reading, UK.

Lui, G., 2008. A database of microwave single-scattering properties for nonspherical ice particles. Bull. Am. Met. Soc., 1563–1570.

Okamoto, K., McNally, A. P., Bell, W., 2014. Progress towards the assimilation of all-sky infrared radiances: an evaluation of cloud effects. Q. J. R. Meteorol. Soc. 140, 1603–1614.

Weston, P., Geer, A., Bormann, N., 2019. Investigations into the assimilation of AMSU-A in the presence of cloud and precipitation. EUMETSAT/ECMWF Fellowship Programme Research Report No.50.